RSC Advances

PAPER

View Article Online
View Journal | View Issue

Cite this: *RSC Adv.*, 2020, **10**, 4032

Enhancement of photocatalytic hydrogen evolution with catalysts based on carbonized MOF-5 and g-C_3N_4†

Malgorzata Aleksandrzak,* Krzysztof Sielicki and Ewa Mijowska

The study presents enhancement of photocatalytic hydrogen generation after metal–organic framework (MOF5) carbonization at 700 °C and its utilization as a co-catalyst of graphitic carbon nitride (gCN). Thermal treatment of MOF5 affected the formation of ZnO nanoparticles which played the role of co-catalyst for H_2 evolution. Moreover, significant band-gap narrowing of MOF5 was observed, which also affected the narrowing of the hybrid band gap. The appropriate conduction band position of the carbonized MOF allowed photogenerated electron transfer from gCN to the carbonized MOF, hence, improving the separation of the charge carriers and reducing the overpotential for H_2 generation. The mechanism of the photocatalytic process was also discussed.

Received 14th October 2019
Accepted 20th December 2019

DOI: 10.1039/c9ra08388j

rsc.li/rsc-advances

Introduction

Metal–organic frameworks (MOFs) are a very extensive group of zeolite-like materials with aesthetic shapes, comprised of metal ions or ion clusters and organic linkers.[1] These materials can be applied to many fields: gas adsorption,[2,3] sensing,[4,5] sorption,[6,7] gas separation,[3,8] and catalysis.[9] MOFs have high microporous volume, tunable pore structure and high metal content which leads to potentially valuable active sites. Especially in photocatalysis organic linkers can serve as an antenna to absorb light in the process of linker-to-metal-cluster charge transfer (LCCT), which can provide possible advantages in combination with other co-catalysts.[10]

Recently, carbon-based metal-free materials, like graphitic carbon nitride (g-C_3N_4) have become popular as photocatalysts. Due to its low band gap energy (2.7 eV), depending on structural variations or the presence of adatoms,[11] this material can be excited *via* visible light. Furthermore, it can be easily synthesized in one-step polymerization from cheap precursors such as cyanamide, urea, thiourea, melamine and dicyandiamide.[12] However, pristine g-C_3N_4 suffers from low sunlight conversion efficiency, due to limited visible light absorption, low surface area and grain boundary effects. Nevertheless, the optimization has been proceeded by morphology manipulation,[13] chemical doping, reduction of the grain size,[11] bacterial etching for delamination,[14] flash frozen exfoliation,[15] surface amino-groups regulation[16] and metal, metal oxide, halide or noble metal heterojunctions.[12–17]

Recently, MOFs/g-C_3N_4 based materials have been emerged. L. Tian *et al.* have synthesized ZIF-8/g-C_3N_4 composite *via* three-step method for solar-driven photocatalytic hydrogen evolution. The composite demonstrated efficient utilization of visible light and improvements in charge transportation and redox capability.[18] On the other hand, Pandiaraj *et al.* used carbonized MOF-5 as a scaffold for g-C_3N_4 polymerization.[19] The designed electrocatalyst, showed enhanced oxygen reduction reaction (ORR) activity in comparison to the commercial Pt catalyst. In another study, synergetic effect between mesoporous carbon and g-C_3N_4 was observed.[20] Y. Gong *et al.* used nitrogen doped ZIF-8/g-C_3N_4 composites for bisphenol A degradation under visible light. In this work, Schottky contact between ZIF-NC and g-C_3N_4 facilitated the charge separation of g-C_3N_4.[20] W. Gu *et al.* successfully synthesized g-C_3N_4/MIL-101 with remarkable catalytic performance for ORR, with high selectivity and H_2O_2 yield.[21] Synthesis and photocatalysis of g-C_3N_4/UiO-66 was presented by X. Zhang *et al.*[22] The material showed improved oxidation of Rhodamine B due to the enhanced separation of photoexcited-electron–hole pairs.[23] Huang *et al.* presented heterojunction of g-C_3N_4 with MIL-53(Fe) with enhanced photocatalytic activity for Cr(VI) reduction under visible light. The study confirmed enhanced separation of photoexcited carriers after combination MOF with g-C_3N_4.[24]

Moreover, there is a lack of information in the current state of the art, how the application of the carbonized MOF5 and g-CN would influence the charge separation of photoexcited electron–hole pairs and the position of band edges for H_2 generation. Therefore, here we present the utilization of MOF5 carbonized at 700 °C for modification of graphitic carbon

Department of Physicochemistry of Nanomaterials, Faculty of Chemical Technology and Engineering, West Pomeranian University of Technology, Szczecin, Piastow Ave. 42, 71-065 Szczecin, Poland. E-mail: mwojtoniszak@zut.edu.pl

† Electronic supplementary information (ESI) available. See DOI: 10.1039/c9ra08388j

nitride and detailed characterization of the impact of the structural, optical and electronic properties on the photocatalytic hydrogen evolution is reported. The mechanism of the photocatalytic process is also discussed.

Results and discussion

Fig. 1 presents SEM and TEM images of MOF5, carbonized MOF5 (CMOF700) and their hybrids with graphitic carbon nitride. SEM image of MOF5 presents typical, with regular cubic structure and flat surface. Its carbonization at 700 °C affected formation of ZnO nanoparticles, which were extracted on the surface of porous carbon cubes (Fig. 1b–d). TGA analysis revealed that CMOF700 is composed of 68 wt% of these nanoparticles (Fig. 3). The distance between the two adjacent planes, estimated from the lattice fringes (Fig. 1d), is found to be 0.28 nm and 0.26 nm, corresponding to (1 0 0) and (0 0 2) plane, respectively. As a result of long term sonication of CMOF700 with graphitic carbon nitride, the cubic frameworks of the carbonized MOF fall apart and finally, the porous carbon flakes with ZnO nanoparticles conjugated with gCN were formed (Fig. 1e–h). According to TEM analysis, the diameters of ZnO nanoparticles were in the range of 5–45 nm, with dominating fraction of 24 nm. EDX spectra and elemental mapping of the samples are presented in Fig. S1–S4.† From the elemental mapping it could be observed that in MOF5 and MOF5–gCN (Fig. S1 and S2†) Zn atoms are homogeneously distributed on the whole surface of the analyzed area, while carbonization at 700 °C resulted in the formation of ZnO particles with tendency to form aggregates (Fig. S3 and S4†).

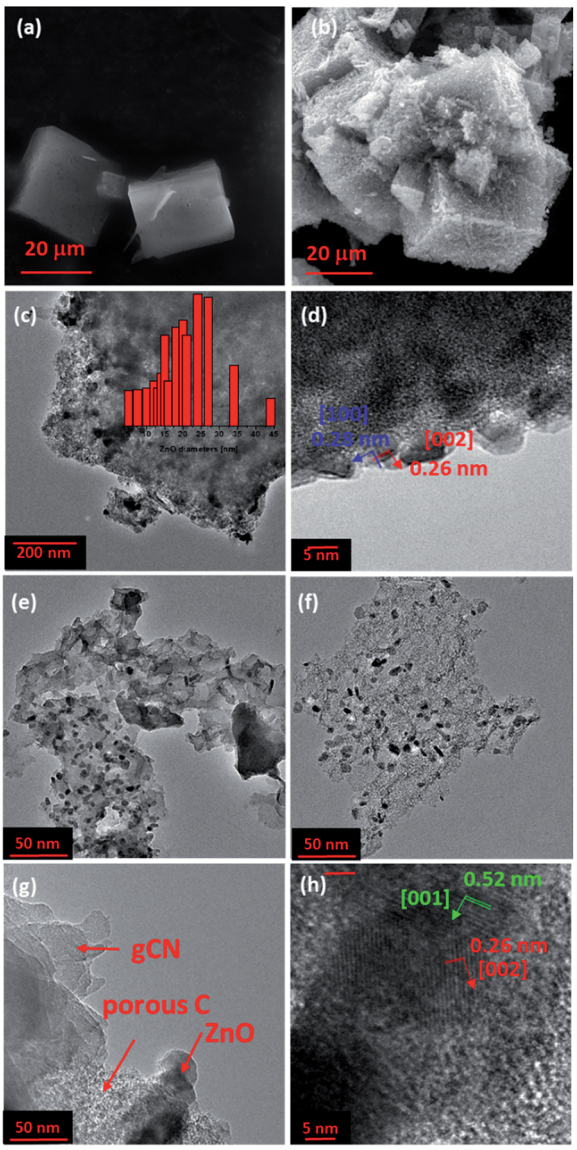

Fig. 1 SEM images of MOF5 (a) and CMOF700 (b). TEM images of CMOF700 (c and d) and CMOF700–gCN (e–h). The inset in image (c) presents ZnO nanoparticles size distribution in CMOF700.

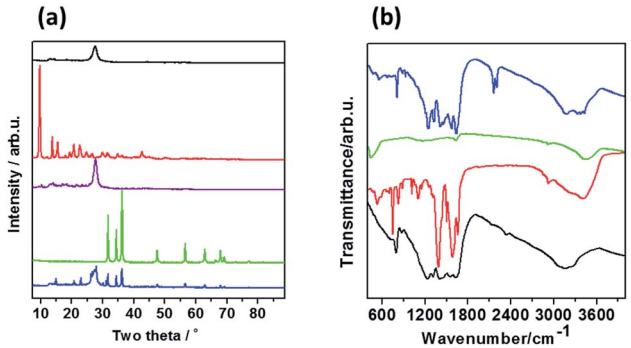

Fig. 2 (a) XRD patterns and (b) FTIR spectra of gCN (black line), MOF-5 (red line), CMOF700 (green line), MOF5–gCN (purple line) and CMOF700–gCN (blue line).

The crystal structure of the prepared samples was characterized with XRD analysis and results are shown in Fig. 2a. gCN presents typical XRD pattern with (002) and (100) crystal planes (JCPDS 87-1526) at two-theta of 13.1° and 27.6°, which are attributed to the condensed tri-*s*-triazine units and the graphitic structure, respectively.[25,26] XRD pattern of MOF5 shows characteristic reflections at 9.77°, 13.87°, 15.56°, 17.95°, 19.41°, 20.74°, 22.66°, 24.81°, 26.68°, 28.49°, 29.88°, 31.69°, 33.11°, 34.89°, 36.16°, 37.47°, 38.55°, 40.33°, 41.03°, 42.25°, 42.64°, 43.64°, 44.92° and 50.22°. According to CCDC – 256965 card,

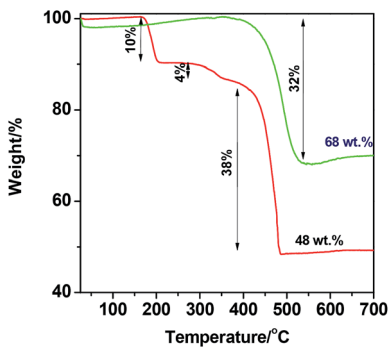

Fig. 3 TGA curves of MOF5 (red line) and CMOF700 (green line) measured under air flow.

those reflections correspond to the following planes: (022), (004), (024), (333), (044), (244), (335), (117), (137), (337), (446), (228), (119), (139), (177), (159), (359), (1111), (179), (3311), (0012), (0212), (3511), (688), (6810), respectively.[27] After gCN coupling with MOF5, reflections at 2-theta of 9.81°, 13.97°, 15.53°, 18.07°, 19.42°, 20.72° and 24.61° appeared from the presence of MOF5, indicating effective functionalization. Thermal treatment of MOF5 at 700 °C resulted in significant changes in XRD pattern, showing phase transformation. The reflections of CMOF700 arise at 31.8°, 34.4°, 36.3°, 47.5°, 56.6°, 62.9°, 66.4°, 67.9° and 69.1°, indicating that nanoparticles deposited at carbon layers, visualized with TEM, are composed of hexagonal zinc oxide and they are attributed to (100), (002), (101), (102), (110), (103), (200), (112) and (201) crystal planes. XRD pattern of CMOF700–gCN is composed of peaks attributed to gCN and CMOF700 indicating successful hybridization of these two components.

FTIR spectra presented in Fig. 2b show that gCN has few characteristic bands related to CN-heterocyclic (809 cm^{-1}), C–N (1237, 1330 and 1410 cm^{-1}), C=N (1565, 1644 cm^{-1}) and NH_2 (3150 cm^{-1}).[23] In the spectrum of MOF5 we can observe characteristic bands at 532, 745, 1104, 1387, 1575, 2930 and 3425 cm^{-1} are observed what is fully consistent with the literature.[28–30] After MOF5 carbonization, most of the peaks disappear, as a result of thermal decomposition of organic ligand molecules, and only weak peaks can be noticed at 1600 cm^{-1} (C=C) and 3425 cm^{-1} (–OH). The combination of gCN and CMOF700 show that all of the peaks related to gCN are observed and two additional peaks at 2160 and 2210 cm^{-1}, corresponding to C–N, are detected.

In order to estimate the chemical composition of MOF5 and carbonized MOF5, thermogravimetric analysis in air flow was conducted (Fig. 3). Black line corresponds to TGA curve of MOF5, where first weight loss at temperature range of 160–215 °C is attributed to the removal of adsorbed water and residual solvent molecules (10 wt%). The second weight loss at 270–370 °C is related to the thermal decomposition of organic ligand molecules (4 wt%), while the third weight loss occurred at 380–490 °C and is attributed to thermal decomposition of the carbon skeleton (38 wt%).[31] The decomposition of the carbon skeleton in CMOF700 (red line) occurs at temperature range of 380–550 °C (32 wt%). Additionally, a minor growth of the CMOF700 weight, probably due to the adsorption of the gas, at 120–320 °C (2 wt%) occurred. 48 wt% and 68 wt% residues of MOF5 and CMOF700, respectively, correspond to zinc oxide remained after the thermal treatment. Hence, MOF5 is composed of 39 wt% of Zn element.

The nitrogen adsorption–desorption isotherms are employed to demonstrate specific surface area and pore size distribution of the prepared MOFs and graphitic carbon nitride. As shown in Fig. 4a, both samples exhibit typical type IV isotherms with an H-type hysteresis loop, suggesting the mesoporous characteristics.[31] The pore size distribution of MOF5, determined by the DFT method, shows relatively higher volume of pores in micropore range than CMOF700 (Fig. 4b). The specific surface area of the materials and volume of the pores are presented in Table 1. Carbonization of MOF5 and further

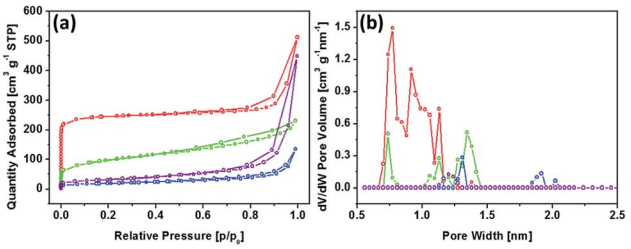

Fig. 4 Nitrogen adsorption–desorption isotherms at 77 K (a) and DFT adsorption pore size distribution (b) for MOF5 (red), CMOF700 (green), MOF5–gCN (purple) and CMOF700–gCN (blue).

combining with gCN resulted in successive decrease in specific surface area and pore volume.[32,33]

The photocatalytic hydrogen evolution, performed in 20 mL of water containing 10 mg of the photocatalyst and irradiated with 150 W Xe lamp with A.M. 1.5G filter, is presented in Fig. 5a. The modification of graphitic carbon nitride with MOF5 influenced slight increase in H_2 evolution rate. 11.6 μmol g^{-1} of H_2 produced after 4 h while bulk gCN produced 10.04 μmol g^{-1} of hydrogen. Interestingly, in the presence of the catalyst based on CMOF700 and gCN a noticeable improvement of the photocatalytic activity was revealed. Here, 232.72 μmol g^{-1} of H_2 was produced after 4 h of irradiation. First factor, which explains this behavior is attributed to the formation of ZnO nanoparticles. They are suitable for hydrogen generation, as its conduction band edge is more negative than the potential of H^+ reduction.[34] The nanocomposite CMOF700–gCN was further used for determination of apparent quantum efficiency at 426 nm ± 20 nm. The amount of the evolved hydrogen was 180 μmol g^{-1} and AQE was found to be 0.82%.

In order to evaluate the photostability of CMOF700–gCN, four cycles of the photocatalytic hydrogen evolution were performed (Fig. 5b). The experiment showed that the photocatalytic activity of the catalyst was stable for the entire four cycles, however, a minor decrease was observed. The H_2 evolution rate barely dropped by 3.1% after four cycles. The minor decrease might be attributed to the consumption of lactic acid which was successively oxidized during the photocatalytic reaction.[35]

Generally, the key factor, which contributes to the photocatalytic activity of the semiconductor is absorption and utilization of light. Hence, we used diffuse reflectance UV-vis

Table 1 BET specific surface area and pore volume of MOF5, CMOF700 and CMOF700–gCN

Sample	BET surface area [m^2 g^{-1}]	Pore volume [cm^3 g^{-1}]
gCN	139.8	0.131
MOF5	961.4	0.395
CMOF700	345.3	0.147
MOF5–gCN	110.3	0.131
CMOF700–gCN	65.4	0.038

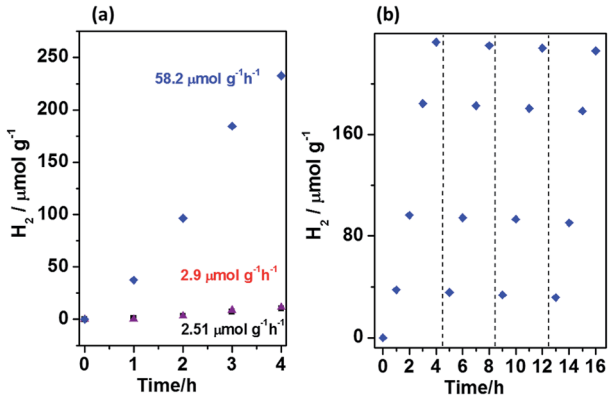

Fig. 5 (a) Photocatalytic hydrogen evolution catalyzed by gCN (black), MOF5–gCN (purple) and CMOF700–gCN (blue). (b) Stability of CMOF700–gCN during four cycles of prolonged photocatalytic hydrogen evolution reaction. Both graphs are based on the experiments conducted in 20 mL of water with 2 mL of lactic acid containing 0.01 g of the photocatalyst under simulated solar light (150 W Xe lamp using an A.M. 1.5G filter).

spectroscopy to characterize optical properties and determine the band gap energy of the samples (Fig. 6a). Graphitic carbon nitride presents typical DRS spectrum with absorption edge at 463 nm, which corresponds to the band gap of 2.68 eV. The absorption edge of MOF5 is located at ~323 nm and corresponds to E_g of 3.84 eV. The carbonization resulted in significant red-shifting of the absorption edge to 492 nm (E_g = 2.52 eV), allowing absorption of visible light. The narrowed band gap of CMOF700 in comparison to MOF5 is firstly attributed to the formation of ZnO nanoparticles. However, the band gap of ZnO is ~3.3 eV.[36] The significant decrease in the band gap to 2.52 eV is related to the presence of porous carbon material (~15 wt%). The interaction between carbon nitride and CMOF700 resulted in the enhancement of the absorption of visible light and shifting of the absorption edge to 512 nm. It corresponds to E_g = 2.42 eV. These data illustrate positive effect of the carbonization process of metal–organic framework on the absorption of visible light and thereby the photocatalytic activity in hydrogen evolution reaction.

In order to estimate the position of a conduction band edge (CB), a flat-band potential can be determined from the Mott–Schottky analysis. Fig. 6b presents Mott–Schottky plots of gCN, MOF5, CMOF700 and CMOF700–gCN. The potential-dependent electrochemical impedance of the samples in the darkness, at a frequency of 20 kHz and an amplitude of 5 mV, was measured. This measurement is then employed to derive their space charge capacitance that is afterwards plotted as a function of the applied potential according to the Mott–Schottky formula:[37]

$$\frac{1}{C^2} = \frac{2}{\varepsilon\varepsilon_0 A^2 e N_D}\left(V - V_{fb} - \frac{k_B T}{e}\right) \quad (1)$$

The flat-band potential is derived from the intercept of the linear curve in the Mott–Schottky plot. The flat-band potentials of gCN, MOF5, CMOF700 and CMOF700–gCN are −1.13, −1.17, −0.84 and −0.80 V *vs.* SCE, respectively. The flat-band potential of the thermal-threated MOF is more positive in comparison to the pristine MOF5. This is the effect of zinc oxide formation and extraction on the porous carbon surface. Moreover, after interaction of CMOF700 with graphitic carbon nitride, the flat band shifts even more to the positive potential. It can be explained by pulling of the Fermi level toward positive potential as soon as CMOF700 contacts with the graphitic carbon nitride, leading to form a new balance.[38] This indicates strong diminishing of the overpotential for water reduction reaction and enhanced reduction ability of CMOF700–gCN hybrid compared to the pristine gCN or MOF5–gCN. Basing on the band gap energy values and flat band potentials, valence band (VB) and conduction band (CB) edge levels were calculated and the band structure diagram was drawn (Fig. 6c).

Photoluminescence spectroscopy was used to examine the separation ability of the photogenerated charge carriers of gCN, MOF5–gCN and CMOF700–gCN (Fig. 7a). The study revealed that the PL intensity of gCN modified with MOF5 is lower than that of the pristine gCN, while CMOF700 exhibits even lower PL

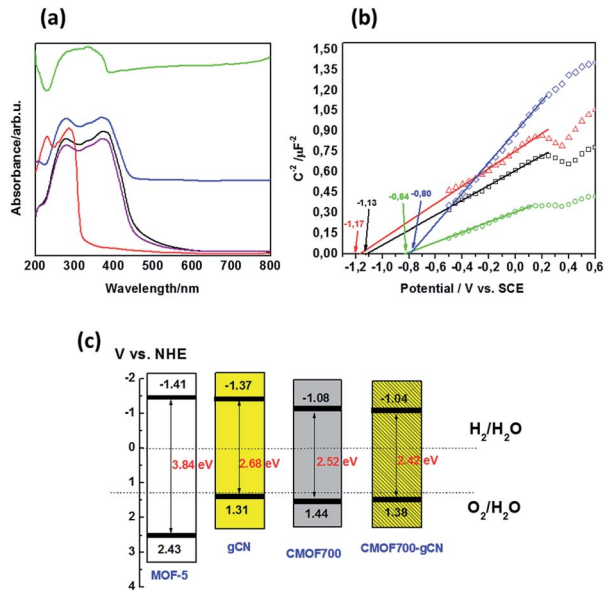

Fig. 6 (a) DRS spectra, (b) Mott–Schottky plots of gCN (black line), MOF5 (red line), MOF5–gCN (purple line), CMOF700 (green line) and CMOF700–gCN (blue line). (c) Band structure diagram of MOF5, gCN, CMOF700 and CMOF700–gCN.

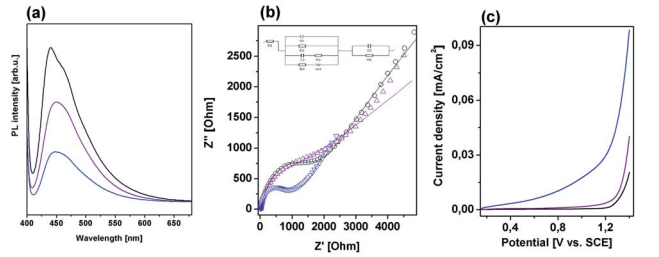

Fig. 7 (a) PL spectra, (b) EIS spectra and (c) LSV curves of gCN (black line), MOF5–gCN (purple line) and CMOF700–gCN (blue line).

emission, indicating significant improvement of the charge carrier separation. For deeper understanding of the transport behavior of the photogenerated charge carriers, the EIS and LSV technique were employed under irradiation of 420–700 nm (Fig. 7b and c). It is known that a smaller arc radius of the EIS Nyquist plot corresponds to an effective separation of photogenerated electron–hole pairs and fast interfacial charge transfer.[38] The arc radius on EIS Nyquist plot of CMOF700–gCN is smaller than that of gCN and MOF5–gCN. This suggests that it owns a more effective photogenerated carrier separation and fast interfacial charge transfer capability. The same trend was observed in the results of the LSV response. The signal from graphitic carbon nitride was successfully enhanced when it was modified with MOF5 and CMOF700 indicating the efficient separation and transport properties. These results are in good agreement with PL spectroscopy. The enhanced separation ability of CMOF700–gCN is related to the band alignment of these two components (Fig. 6c). Since conduction band minimum (CBM) and valence band maximum (VBM) of CMOF700 are more positive than that of gCN, the photogenerated electrons are transferred from gCN to the carbonized MOF. Moreover, the porous carbon layers can mediate in electron transferring from graphitic carbon nitride to zinc oxide nanoparticles. Simultaneously, photon-induced holes can travel from VBM of CMOF700 to VBM of graphitic carbon nitride yielding enhanced separation of charge carriers and improved photocatalytic activity for hydrogen generation.

The above analysis clearly indicates that thermal treatment of the metal–organic framework (MOF5) at 700 °C followed by conjugation with graphitic carbon nitride for improvement of photocatalytic hydrogen generation is highly reasonable. Although, the specific surface area of CMOF700 drastically decreased in comparison with MOF5, the material exhibits much improved co-catalytic properties for hydrogen generation. This is attributed to the following aspects: (i) pyrolysis of MOF5 at 700 °C resulted in the formation of porous carbon layers and ZnO nanoparticles acting as mediator in electron transferring and co-catalyst with suitable CBM for hydrogen evolution reaction, respectively; (ii) band gap narrowing from 3.84 eV (MOF5) to 2.52 eV (CMOF700) and from 2.68 eV (gCN) to 2.42 eV (CMOF700–gCN) indicative of improved visible light harvesting; (iii) enhanced separation of charge carriers, since porous carbon layers could accept photoinduced electrons from gCN and further mediate in migration to ZnO nanoparticles, simultaneously photogenerated holes transferred from CMOF700 to gCN, and finally, (iv) more positive flat-band potential of CMOF700 in comparison to MOF5 indicating reduced overpotential for hydrogen generation.

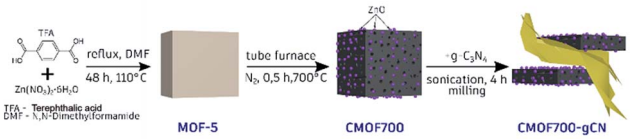

Scheme 1 Synthesis procedure of CMOF700 and CMOF700–gCN.

After detailed analysis, the mechanism of the photocatalytic reaction with CMOF700–gCN can be proposed. When the photocatalyst was irradiated with simulated solar light graphitic carbon nitride and ZnO from the carbonized MOF5 were excited leading to transferring of the electrons to the conduction bands and leaving holes in the valence bands. The photoexcited electrons could migrate from gCN in two pathways: (i) to the surface reaction sites leading to photocatalytic H^+ reduction and evolution of hydrogen, and (ii) to the surface of porous carbon flakes which played a role of mediator in electron migration to ZnO nanoparticles. The second pathway is possible because CBM of gCN is more negative than the CBM of CMOF700. The photogenerated electrons of CMOF700 can migrate to the surface reaction sites allowing H_2 generation. Simultaneously, the holes from valence band of the carbonized MOF could migrate to VB of graphitic carbon nitride, as its valence band maximum (VBM) is more positive than VBM of gCN. The holes from both co-catalysts were consumed for oxidation of lactic acid used as the sacrificial reagent. The weaker co-catalytic properties of MOF5 are attributed to the wider band gap which prevents visible light absorption and inferior separation and transport properties arising from the band alignment in relation to graphitic carbon nitride.

Conclusions

In summary, metal–organic framework (MOF5) was carbonized at 700 °C and used as co-catalyst of graphitic carbon nitride for photocatalytic hydrogen evolution. The carbonized MOF5 was found to significantly enhance the efficiency of H_2 production when compared to pristine gCN or gCN modified with MOF5. It was the effect of formation of ZnO nanoparticles, band gap narrowing, enhanced separation of charge carriers and reduced overpotential for H_2 evolution.

Experimental

1. Materials

Zinc nitrate hexahydrate ($Zn(NO_3)_2 \cdot 6H_2O$), terephthalic acid ($C_6H_4(COOH)_2$) were purchased from Sigma Aldrich. *N*,*N*-Dimethylformamide was purchased from Chempur (Poland).

2. Synthesis

2.1. MOF5. The MOF5 was prepared according to literature.[39] Hence, 3.3 mol of zinc nitrate hexahydrate and 1.79 mol terephthalic acid were dissolved in 4.93 mol *N*,*N*-dimethylformamide (DMF). The mixture was homogenized and transferred into a flask under reflux for 48 h at the temperature of 110 °C. Finally, cubic crystals were vacuum dried at 110 °C for 2 h to remove the solvent molecules. Next, the ceramic boat containing white powder of MOF5 was inserted into center of a tubular furnace. The furnace was heated from room temperature to 700 °C and maintained for 0.5 h under Ar flow to obtain CMOF700.

2.2. Graphitic carbon nitride. Graphitic carbon nitride (gCN) was prepared *via* calcination of urea in a muffle furnace at

550 °C for 4 h in air. The temperature was achieved with a heating rate of 2 °C min^{-1}. After reaction, the furnace was cooled down to room temperature in air atmosphere.

2.3. MOF5–gCN and CMOF700–gCN. 4 mg of MOF5 or CMOF700 was added to 36 mg of bulk graphitic carbon nitride and 10 mL of water. Next, the mixture was sonicated for 4 h, followed by water evaporation. Finally, the powder product was milled in mortar to obtain MOF5–gCN and CMOF700–gCN. Synthesis of CMOF700 and CMOF700–gCN is presented on Scheme 1.

3. Characterization

The morphology of the samples was examined with transmission electron microscopy (TEM, Tecnai F30). The crystal structure of the samples was analyzed with X-ray diffraction using X'Pert Philips Diffractometer with Cu lamp. Brunauer–Emmett–Teller (BET) specific surface area and pore volume were measured by nitrogen sorption in the temperature of liquid nitrogen using a Micromeritics ASAP 2460. The pore size distribution of each sample was calculated using non-local density functional theory (NLDFT), from the desorption branch of the isotherms. Thermogravimetric analysis was performed on the SDT Q600 Simultaneous TGA/DSC in argon at heating rate of 10 °C min^{-1}. FTIR spectroscopy measurements were carried out on Nicolet 6700 FT-IR spectrometer. The room temperature photoluminescence (PL) spectra were recorded on fluorescence spectrophotometer F 7000 (Hitachi) with 380 nm excitation wavelength. The optical properties of the materials were characterized by means of diffuse reflectance spectroscopy (DRS), using Jasco (Japan) spectrometer. Band gap energy values were calculated from equation

$$E_g = hc/\lambda. \quad (2)$$

The electrochemical tests were performed with BioLogic VMP-3 potentiostat station in a three-electrode cell according to our previous method.[40] Linear sweep potentiometry and electrochemical impedance spectroscopy measurements were conducted by Autolab PGSTAT302N potentiostat in a 3-electrode test cell with a platinum wire as counter electrode and saturated calomel electrode as reference. LSV test was performed from 0.15 V to 1.4 V *vs.* SCE with 50 mV s^{-1} scan rate. EIS was measured at frequency range of 100 kHz to 0.01 Hz with 5 mV AC signal amplitude. 0.5 M sodium sulfate was used as the electrolyte.

4. Photocatalytic hydrogen evolution

Photocatalytic process of hydrogen evolution was carried out in an outer irradiation-type reactor (Pyrex glass) connected to argon. 10 mg of a photocatalyst was dispersed in 20 mL of water and sonicated for 1 h. After that, 2 mL of lactic acid was poured and the reactor was purged with argon to remove air, followed by irradiation with 150 W Xe lamp with an air mass filter (A.M. 1.5G). The photocatalytic H_2 evolution rate was analyzed using Young Lin 6500 gas chromatograph (GC, Micro TCD detector, HayeSep A-Valco PLOT Capillary Columns and Ar as a carrier). Four cycles of experiments were carried out to investigate the stability of the photocatalyst. Each test was carried out for 4 hours under the irradiation. After each test, the gaseous products were evacuated, and the reactor was purged with argon.

The apparent quantum efficiency at $\lambda_0 = 426$ nm (±20 nm) was calculated for CMOF700–gCN photocatalyst. The average intensity of irradiation was determined to be 2.6 mW cm^{-2} and the irradiation area was 4.9 cm^2. The number of incident photons (N) in 4 hours is 3.93×10^{-20} as calculated by eqn (3):

$$N = \frac{E\lambda}{hc} \quad (3)$$

The amount of H_2 molecules generated in 4 hours was 1.8 μmol. The quantum efficiency is calculated from eqn (4):

$$\mathrm{AQE} = \frac{2 \times \text{the number of evolved } H_2 \text{ molecules}}{\text{the number of incident photons}} \quad (4)$$

Conflicts of interest

There are no conflicts to declare.

Acknowledgements

This work was financially supported by the National Science Center, Poland, under SONATA program (no. 2015/19/D/ST5/01920).

Notes and references

1 T. Dutta, K. Kim, R. Brown, Y. Kim and D. Boukhvalov, Metal-organic framework and Tenax-TA as optimal sorbent mixture for concurrent GC-MS analysis of C1 to C5 carbonyl compounds, *Sci. Rep.*, 2018, **8**(1), 5033.
2 C. Trickett, A. Helal, B. Al-Maythalony, Z. Yamani, K. Cordova and O. Yaghi, The chemistry of metal–organic frameworks for CO2 capture, regeneration and conversion, *Nat. Rev. Mater.*, 2017, **2**(8), 17045.
3 Y. Belmabkhout, P. Bhatt, K. Adil, R. Pillai, A. Cadiau, A. Shkurenko, G. Maurin, L. Gongping, W. Koros and M. Eddaoudi, Natural gas upgrading using a fluorinated MOF with tuned H2S and CO2 adsorption selectivity, *Nat. Energy*, 2018, 1059.
4 H. Shiozawa, B. Bayer, H. Peterlik, J. Meyer, W. Lang and T. Pichler, Doping of metal–organic frameworks towards resistive sensing, *Sci. Rep.*, 2017, **7**(1), 2439.
5 L. Pan, G. Liu, W. Shi, J. Shang, W. Leow, Y. Liu, Y. Jiang, S. Li, X. Chen and R. Li, Mechano-regulated metal–organic framework nanofilm for ultrasensitive and anti-jamming strain sensing, *Nat. Commun.*, 2018, **9**(1), 3813.
6 S. Wang, J. Lee, M. Wahiduzzaman, J. Park, M. Muschi, C. Martineau-Corcos, A. Tissot, K. Cho, J. Marrot, W. Shepard, G. Maurin, J. Chang and C. Serre, A robust large-pore zirconium carboxylate metal–organic framework

for energy-efficient water-sorption-driven refrigeration, *Nat. Energy*, 2018, **3**(11), 985–993.

7 S. Wang, J. Lee, M. Wahiduzzaman, J. Park, M. Muschi, C. Martineau-Corcos, A. Tissot, K. Cho, J. Marrot, W. Shepard, G. Maurin, J. Chang and C. Serre, A robust large-pore zirconium carboxylate metal–organic framework for energy-efficient water-sorption-driven refrigeration, *Nat. Energy*, 2018, **3**(11), 985–993.

8 G. Liu, V. Chernikova, Y. Liu, K. Zhang, Y. Belmabkhout, O. Shekhah, C. Zhang, S. Yi, M. Eddaoudi and W. Koros, Mixed matrix formulations with MOF molecular sieving for key energy-intensive separations, *Nat. Mater.*, 2018, **17**(3), 283–289.

9 X. Zhang, Z. Huang, M. Ferrandon, D. Yang, L. Robison, P. Li, T. Wang, M. Delferro and O. Farha, Catalytic chemoselective functionalization of methane in a metal−organic framework, *Nat. Catal.*, 2018, **1**(5), 356–362.

10 Y. Li, H. Xu, S. Ouyang and J. Ye, Metal–organic frameworks for photocatalysis, *Phys. Chem. Chem. Phys.*, 2016, **18**(11), 7563–7572.

11 Y. Zhang, Z. Schnepp, J. Cao, S. Ouyang, Y. Li, J. Ye and S. Liu, Biopolymer-Activated Graphitic Carbon Nitride towards a Sustainable Photocathode Material, *Sci. Rep.*, 2013, **3**(1), 2163.

12 Z. Zhao, Y. Sun and F. Dong, Graphitic carbon nitride based nanocomposites: a review, *Nanoscale*, 2015, **7**(1), 15–37.

13 L. Cui, J. Song, A. F. McGuire, S. Kang, X. Fang, J. Wang, C. Yin, X. Li, Y. Wang and B. Cui, Constructing Highly Uniform Onion-Ring-like Graphitic Carbon Nitride for Efficient Visible Light-Driven Photocatalytic Hydrogen Evolution, *ACS Nano*, 2018, **12**(6), 5551–5558.

14 S. Kang, W. Huang, L. Zhang, M. He, S. Xu, D. Sun and X. Jiang, Moderate Bacterial Etching Allows Scalable and Clean Delamination of g-C3N4 with Enriched Unpaired Electrons for Highly Improved Photocatalytic Water Disinfection, *ACS Appl. Mater. Interfaces*, 2018, **10**(16), 13796–13804.

15 S. Kang, L. Zhang, C. Yin, Y. Li, L. Cui and Y. Wang, Fast flash frozen synthesis of holey few-layer g-C3N4 with high enhancement of photocatalytic reactive oxygen species evolution under visible light irradiation, *Appl. Catal., B*, 2017, **211**, 266–274.

16 S. Kang, M. He, M. Chen, Y. Liu, Y. Wang, Y. Wang, M. Dong, X. Chang and L. Cui, Surface Amino Group Regulation and Structural Engineering of Graphitic Carbon Nitride with Enhanced Photocatalytic Activity by Ultrafast Ammonia Plasma Immersion Modification, *ACS Appl. Mater. Interfaces*, 2019, **11**(16), 14952–14959.

17 J. Fu, J. Yu, C. Jiang and B. Cheng, g-C3N4-Based Heterostructured Photocatalysts, *Adv. Energy Mater.*, 2018, **8**, 1701503.

18 L. Tian, X. Yang, Q. Liu, F. Qu and H. Tang, Anchoring metal-organic framework nanoparticles on graphitic carbon nitrides for solar-driven photocatalytic hydrogen evolution, *Appl. Surf. Sci.*, 2018, **455**, 403–409.

19 S. Pandiaraj, H. Aiyappa, R. Banerjee and S. Kurungot, Post modification of MOF derived carbon via g-C3N4 entrapment for an efficient metal-free oxygen reduction reaction, *Chem. Commun.*, 2014, **50**(25), 3363–3366.

20 Y. Gong, X. Zhao, H. Zhang, B. Yang, K. Xiao, T. Guo, J. Zhang, H. Shao, Y. Wang and G. Yu, MOF-derived nitrogen doped carbon modified g-C_3N_4 heterostructure composite with enhanced photocatalytic activity for bisphenol A degradation with peroxymonosulfate under visible light irradiation, *Appl. Catal., B*, 2018, **233**, 35–45.

21 W. Gu, L. Hu, J. Li and E. Wang, Hybrid of g-C3N4 Assisted Metal–Organic Frameworks and Their Derived High-Efficiency Oxygen Reduction Electrocatalyst in the Whole pH Range, *ACS Appl. Mater. Interfaces*, 2016, **8**(51), 35281–35288.

22 X. Zhang, Y. Yang, W. Huang, Y. Yang, Y. Wang, C. He, N. Liu, M. Wu and L. Tang, g-C3N4/UiO-66 nanohybrids with enhanced photocatalytic activities for the oxidation of dye under visible light irradiation, *Mater. Res. Bull.*, 2018, **99**, 349–358.

23 W. Huang, N. Liu, X. Zhang, M. Wu and L. Tang, Metal organic framework g-C3N4/MIL-53(Fe) heterojunctions with enhanced photocatalytic activity for Cr(VI) reduction under visible light, *Appl. Surf. Sci.*, 2017, **425**, 107–116.

24 M. Aleksandrzak, D. Baranowska, T. Kedzierski, K. Sielicki, S. Zhang, M. Biegun and E. Mijowska, Superior synergy of g-C3N4/Cd compounds and Al-MOF-derived nanoporous carbon for photocatalytic hydrogen evolution, *Appl. Catal., B*, 2019, **257**, 117906–117915.

25 A. Thomas, *et al.*, Graphitic carbon nitride materials: variation of structure and morphology and their use as metal-free catalysts, *J. Mater. Chem.*, 2008, **18**, 4893–4908.

26 J. R. Holst and E. G. Gillan, From triazines to heptazines: deciphering the local structure of amorphous nitrogen-rich carbon nitride materials, *J. Am. Chem. Soc.*, 2008, **130**, 7373–7379.

27 L. Huang, H. Wang, J. Chen, Z. Wang, J. Sun, D. Zhao and Y. Yan, Synthesis, morphology control, and properties of porous metal-organic coordination polymers, *Microporous Mesoporous Mater.*, 2003, **58**, 105–114.

28 M. Kim, S. Hwang and J. Yu, Novel ordered nanoporous graphitic C3N4 as a support for Pt–Ru anode catalyst in direct methanol fuel cell, *J. Mater. Chem.*, 2007, **17**(17), 1656–1659.

29 S. Bennabi and M. Belbachir, Synthesis and Characterization of a new hybrid material (MOF-5/Mag-H+) based on a Metal-Organic Framework and a Proton Exchanged Montmorillonite Clay (Maghnite-H+) as catalytic support, *Journal of Materials and Environmental Sciences*, 2017, **8**(12), 4391–4398.

30 K. Rajan, N. Iswarya, M. Kumar and J. Rayappan, Metal Organic Framework (MOF-5) For Sensing of Volatile Organic Compounds, *J. Appl. Sci.*, 2012, **12**(16), 1681–1685.

31 C. Cendrowski, P. Skumial, P. Spera, E. Mijowska, H. Yang, X. Song, T. Yang, Z. Liang, C. Fan and X. Hao, Electrochemical synthesis of flower shaped morphology MOFs in an ionic liquid system and their electrocatalytic application to the hydrogen evolution reaction, *RSC Adv.*, 2014, **4**(30), 15720–15726.

32 L. Zhang, N. Ding, J. Wu, K. Iwasaki, L. Lin, Y. Yamaguchi, Y. Shibayama, J. Shi, H. Wu, Y. Luo, K. Nakata, D. Li, X. Wang, A. Fujishima and Q. Meng, New two-dimensional porous graphitic carbon nitride nanosheets for highly efficient photocatalytic hydrogen evolution under visible-light irradiation, *Catal. Sci. Technol.*, 2018, **8**(15), 3846–3852.

33 Y. Han, P. Qi, S. Li, X. Feng, J. Zhou, H. Li, S. Su, X. Li and B. Wang, A novel anode material derived from organic-coated ZIF-8 nanocomposites with high performance in lithium ion batteries, *Chem. Commun.*, 2014, **50**(59), 8057–8060.

34 M. Gopannagari, D. P. Kumar, H. Park, E. H. Kim, P. Bhavani, D. A. Reddy and T. K. Kim, Influence of surface-functionalized multi-walled carbon nanotubes on CdS nanohybrids for effective photocatalytic hydrogen production, *Appl. Catal., B*, 2018, **236**, 294–303.

35 V. Srikant and D. R. Clarke, On the optical band gap of zinc oxide, *J. Appl. Phys.*, 1998, **83**(10), 5447.

36 Y. C. Chen, K. H. Yang, C. Y. Huang, Z. J. Wu and Y. K. Hsu, Overall photoelectrochemical water splitting at low applied potential over ZnO quantum dots/nanorods homojunction, *Chem. Eng. J.*, 2019, **368**, 746.

37 Y. Gong, H. Yu, S. Chen and X. Quan, Constructing metal-free polyimide/g-C3N4 with high photocatalytic activity under visible light irradiation, *RSC Adv.*, 2015, **5**(101), 83225.

38 M. Sun, Z. Chen, X. Jiang, C. Feng and R. Zeng, Optimized preparation of Co-Pi decorated g-C3N4@ZnO shell-core nanorod array for its improved photoelectrochemical performance and stability, *J. Alloys Compd.*, 2019, **780**, 540–551.

39 S. Yang, T. Kim, J. Im, Y. Kim, K. Lee, H. Jung and C. Park, MOF-Derived Hierarchically Porous Carbon with Exceptional Porosity and Hydrogen Storage Capacity, *Chem. Mater.*, 2012, **24**(3), 464–470.

40 M. Aleksandrzak, D. Baranowska, T. Kedzierski, K. Sielicki, S. Zhang, M. Biegun and E. Mijowska, Superior synergy of g-C_3N_4/Cd compounds and Al-MOF-derived nanoporous carbon for photocatalytic hydrogen evolution, *Appl. Catal., B*, 2019, **257**, 117906–117915.